Measuring finite-frequency body-wave amplitudes and traveltimes

K. Sigloch, G. Nolet

Geophys. J. Int. (2006) **167,** 271–287 doi: 10.1111/j.1365-246X.2006.03116.x

Measuring finite-frequency body-wave amplitudes and traveltimes

Karin Sigloch and Guust Nolet

Princeton University, Geosciences Department, 315 *Guyot Hall, Princeton, NJ* 08544, *USA. E-mail: sigloch@princeton.edu*

Accepted 2006 June 8. Received 2006 June 2; in original form 2005 December 2

SUMMARY

We have developed a method to measure finite-frequency amplitude and traveltime anomalies of teleseismic *P* waves. We use a matched filtering approach that models the first 25 s of a seismogram after the *P* arrival, which includes the depth phases *pP* and *sP*. Given a set of broad-band seismograms from a teleseismic event, we compute synthetic Green's functions using published moment tensor solutions. We jointly deconvolve global or regional sets of seismograms with their Green's functions to obtain the broad-band source time function. The matched filter of a seismogram is the convolution of the Green's function with the source time function. Traveltimes are computed by cross-correlating each seismogram with its matched filter. Amplitude anomalies are defined as the multiplicative factors that minimize the RMS misfit between matched filters and data. The procedure is implemented in an iterative fashion, which allows for joint inversion for the source time function, amplitudes, and a correction to the moment tensor. Cluster analysis is used to identify azimuthally distinct groups of seismograms when source effects with azimuthal dependence are prominent. We then invert for one source time function per group. We implement this inversion for a range of source depths to determine the most likely depth, as indicated by the overall RMS misfit, and by the non-negativity and compactness of the source time function. Finite-frequency measurements are obtained by filtering broad-band data and matched filters through a bank of passband filters.

The method is validated on a set of 15 events of magnitude 5.8 to 6.9. Our focus is on the densely instrumented Western US. Quasi-duplet events ('quplets') are used to estimate measurement uncertainty on real data. Robust results are achieved for wave periods between 24 and 2 s. Traveltime dispersion is on the order of 0.5 s. Amplitude anomalies are on the order of 1 db in the lowest bands and 3 db in the highest bands, corresponding to amplification factors of 1.2 and 2.0, respectively. Measurement uncertainties for amplitudes and traveltimes depend mostly on station coverage, accuracy of the moment tensor estimate, and frequency band. We investigate the influence of those parameters in tests on synthetic data. Along the RISTRA array in the Western US, we observe amplitude and traveltime patterns that are coherent on scales of hundreds of kilometres. Below two sections of the array, we observe a combination of frequency-dependent amplitude and traveltime patterns that strongly suggest wavefront healing effects.

Key words: amplitudes, dispersion, finite frequency, source time function, teleseismic *P* waves, traveltimes.

1 INTRODUCTION

We are exploring how body-wave amplitudes can be exploited more systematically for the purpose of inverting for mantle structure. Amplitude anomalies may be observed when waves are refracted by velocity anomalies in the mantle. Such lensing effects are sensitive mostly to the second spatial derivative of the velocity field. Topography on interfaces like the 670 km boundary may also result in focusing or defocusing of wave energy. Amplitude anomaly data could thus highlight zones of rapid transitions in the mantle and sharpen up the edges of narrow features like slabs or plumes in tomographic pictures. Haddon & Husebye (1978) used a thin-lens approximation to model amplitude and traveltime anomalies under the NORSAR array. Ritsema *et al.* (2002) have studied the global variations of amplitude ratios for long-period *P/PP* and *S/SS* waves. Local geology beneath a receiver, such as a low impedance layer, can cause amplitude anomalies as well. Variations in attenuation—for example, due to spatially varying thickness of the asthenosphere—have occasionally been inverted for using body-wave amplitudes (Iyer & Hirahara 1993, Chapter 15, 24). For all three effects, amplitude and traveltime anomalies show frequency dependencies that contain information about the characteristic scales of the mantle

heterogeneities that the wave interacts with. However, to the best of our knowledge, body-wave amplitude anomalies have not been used in regional and global velocity inversions.

The method we propose can compute amplitude and traveltime measurements in any arbitrary finite-frequency band that is contained within the spectrum of the recorded broad-band seismogram. The full frequency range of the data is used to invert for an earthquake's source time function and to generate the matched filters, that is, our best predictions for the observed broad-band wave shapes. We then filter predicted and observed waveforms to the chosen passbands and extract amplitude and traveltime information for each frequency band separately. This generates the kind of data needed to take full advantage of the finite-frequency theory for body-wave tomography formulated by Dahlen *et al.* (2000). Ray theory predicts focusing effects to be highly non-linear, but Dahlen & Baig (2002) showed that amplitude variations observed at the earth's surface should be much smoother than predicted by ray theory. This raises the prospect of incorporating amplitude data in velocity tomography.

Amplitudes of *P* or *S* waves from deep earthquakes are straightforward to measure (Tibuleac *et al.* 2003), but interference with surface reflections complicates such observations for shallow events. Thus, an important step toward systematically exploiting amplitude data is the development of a method to measure amplitude anomalies for shallow earthquakes at teleseismic distances. This is the purpose and scope of this study. Since shallow events are far more abundant than deep ones they offer the potential for building tomography-sized data sets. The questions we face are: How accurately can amplitude anomalies be measured? How large are they? Are there patterns that indicate the presence of focusing effects?

2 METHOD

2.1 Overview

We start with an overview of the method and provide a more in-depth discussion of its different components in the following sections. The vast majority of earthquakes have their hypocentres located at less than 50 km depth, in which case the initial pulse of the *P* arrival is followed within a few seconds by the depth phases *pP* and *sP*. Our data are broad-band waveforms of ground displacement, and we attempt to model the time window comprising the *P*, *pP*, and *sP* phases (but at most 25 s after the *P* arrival). Figs 1(a) and (b) show a typical seismogram and its predicted Green's function. The *k*th seismogram $\boldsymbol{s}_k$ is modelled as the convolution of its Green's function $\boldsymbol{g}_k$ with the *a priori* unknown source time function $\boldsymbol{f}$:

$$\tilde{\boldsymbol{s}}_k(i) = a_k \sum_j \boldsymbol{g}_k^T(i-j)\boldsymbol{f}(j)$$

or

$$\tilde{\boldsymbol{s}}_k \quad = a_k \boldsymbol{G}_k \boldsymbol{f} = a_k \boldsymbol{u}_k, \tag{1}$$

where $\tilde{\boldsymbol{s}}_k$, $\boldsymbol{g}_k$, $\boldsymbol{f}$, and $\boldsymbol{u}_k$ are column vectors of length N (number of samples). $\boldsymbol{G}_k$ is the $N \times N$ convolution matrix; its rows contain time-shifted and time-reversed copies of $\boldsymbol{g}_k^T$. Green's functions are computed using published moment tensors and a background model as input parameters for Chapman's WKBJ code (Chapman 1978); we use PREM (Dziewonski & Anderson 1981) with attenuation and with the ocean layer replaced by continental crust. Crustal multiples are not modelled explicitly but are absorbed in the source time function if they arrive early. The *amplitude anomaly* a_k acts as a scalar energy correction factor for datum k. An estimate of $\boldsymbol{f}$ is shown in Fig. 1(c), and the corresponding waveform $\boldsymbol{u}_k$ in 1(d). Note that $\tilde{\boldsymbol{s}}_k$ is identical to $\boldsymbol{u}_k$ if one assumes that $a_k = 1$. This assumption is the customary first approximation; by systematically measuring a_k, this work attempts to look beyond the structural assumptions contained in PREM.

Ruff (1989) observed that (1) and $a_k = 1$ usually predict waveforms with shapes that match the shapes of the observed $\boldsymbol{s}_k$ fairly well, but significantly differ in energy content on a station-by-station basis (note that an error in the event magnitude gets absorbed by scaling the source time function). The overall misfit can be reduced substantially if one inverts jointly for $\boldsymbol{f}$ and the a_k from the full data set of K seismograms, $\boldsymbol{s}^T = (\boldsymbol{s}_1^T, \boldsymbol{s}_2^T, , \boldsymbol{s}_K^T)$. This means minimizing the RMS misfit

$$e = \min((\boldsymbol{s} - \tilde{\boldsymbol{s}})^T(\boldsymbol{s} - \tilde{\boldsymbol{s}}))$$

where

$$\tilde{\boldsymbol{s}} = \begin{pmatrix} \tilde{\boldsymbol{s}}_1 \\ \tilde{\boldsymbol{s}}_2 \\ \vdots \\ \tilde{\boldsymbol{s}}_K \end{pmatrix} = \begin{pmatrix} a_1\boldsymbol{G}_1 \\ a_2\boldsymbol{G}_2 \\ \vdots \\ a_K\boldsymbol{G}_K \end{pmatrix} \boldsymbol{f} = \boldsymbol{A}\boldsymbol{f}. \tag{2}$$

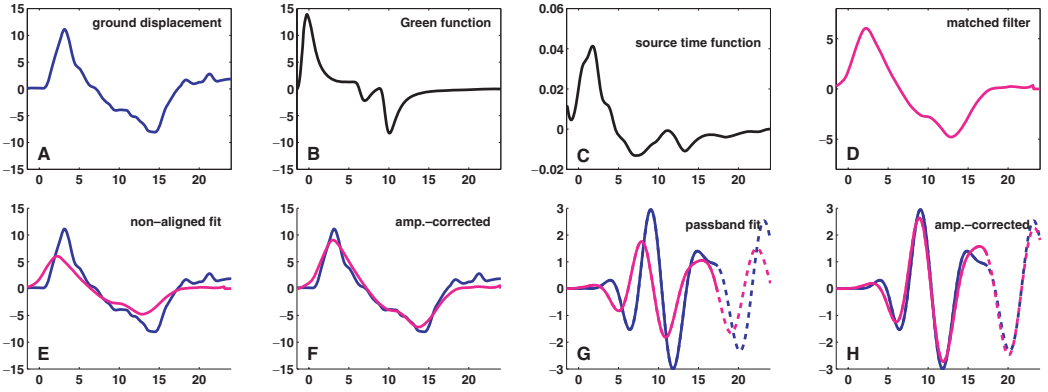

Figure 1. The matched filtering approach to measuring amplitudes and traveltimes. (a) Raw broad-band data: the first 25 s of ground displacement after a teleseismic *P* wave arrival of a shallow event. (b) Synthetic Green's function featuring *P*, *pP*, and *sP* phases. (c) Source time function as computed by jointly deconvolving Green's functions from all data (typically 50–150 *P* wave arrivals). (d) Predicted seismogram, or matched filter: the convolution of B and C. (e) Fit of matched filter to data before temporal alignment and amplitude correction. (f) Fit after correction for (broad-band) traveltime and amplitude anomalies. (g) Bandpassed data and matched filter before temporal alignment and amplitude correction. (h) Fit in passband after correction for (finite-frequency) traveltime and amplitude anomalies. In higher frequency bands we attempt to fit only the first two periods, not the (dashed) oscillations that follow.

Column vectors $\boldsymbol{s}$ and $\tilde{\boldsymbol{s}}$ are length NK, and $\boldsymbol{A}$ is size (NK, N). This is not a standard least squares problem because a_k and $\boldsymbol{f}$ multiply each other in (2). We follow Ruff's recipe for omnilinear inversion, except that we opt for an iterative approach. We also allow for a correction to the published moment tensor values. Details of this deconvolution procedure are described in Section 2.3. Figs 1(e) and (f) illustrate the use of the amplification factor a_k and time delay τ_k to minimize the RMS misfit between the data and the predicted waveform: in 1(e), the data are fitted by $\boldsymbol{u_k}$, whereas in 1(f) $\tilde{\boldsymbol{s}}_k(i) = a_k \boldsymbol{u}_k(i - \tau_k)$ is used. In this example $\tau = 0.8\ s$, and $a_k = 1.2$.

The described procedure is a matched filtering approach, and $\tilde{\boldsymbol{s}}_k$ is called the *matched filter* of seismogram $\boldsymbol{s}_k$. Matched filtering is the optimal strategy for deciding if and where a reference signal $\boldsymbol{x}$ is present in a data stream $\boldsymbol{s}(t)$ that also contains white Gaussian noise. The concept is central to engineering disciplines that involve detection and estimation (radar, sonar, radio communications, etc.). The reference signal $\boldsymbol{x} = \boldsymbol{x}(t;\ \boldsymbol{p})$ is known except for an unknown parameter vector $\boldsymbol{p}$. The solution is to correlate $\boldsymbol{s}$ with a battery of copies (or 'filters') $\boldsymbol{x}$, which are modified by all conceivable values of $\boldsymbol{p}$. If the maximum value of the cross-correlation coefficient is measured for $\boldsymbol{x}(t;\ \boldsymbol{p}_0)$, and if this value exceeds a pre-set threshold, then one decides that the signal has been detected in $\boldsymbol{s}$. The maximum-likelihood estimate for the true $\boldsymbol{p}$ is $\boldsymbol{p}_0$, and $\boldsymbol{x}(t;\ \boldsymbol{p})$ is called the matched filter of $\boldsymbol{s}$ (Flandrin 1999).

In our case, all prior information about seismogram $\boldsymbol{s}_k$ is contained in the Green's function $\boldsymbol{g}_k$ (station and event location, earth model, event depth, moment tensor). Unknown parameters are the source time function $\boldsymbol{f}$, and the amplitudes a_k. Strictly speaking, the traveltime anomalies τ_k are also unknown parameters. The problem of jointly estimating $\boldsymbol{f}$ and a_k can be linearized, but time-shifting is a non-linear operation that we do not want to introduce into the iterative inversion procedure. Instead we estimate traveltimes in separate pre- and post-processing steps. During pre-processing, we time align the raw data using VanDecar & Crosson's method (1990). Once the matched filters are computed, we attempt to recover any remaining delays by cross-correlating each $\tilde{\boldsymbol{s}}_k$ with its $\boldsymbol{s}_k$. The time-shifting and final broad-band amplitude correction from 1(e) to 1(f) are thus done after the source time function inversion has converged, but intermediate estimates for a_k are computed in every iteration. Focal depth estimates in catalogues often come with large uncertainties, and hence source depth is also treated as an unknown. A misestimate in focal depth has considerable impact on the shape of the $\boldsymbol{g}_k$ because it determines the temporal spacing of the P, pP, and sP pulses. These errors directly propagate into the shape of the inverted source time function. We compute source time functions and matched filters for all conceivable depths (between 0 and 60 km, in increments of 1 or 2 km). Decision for the 'best' depth is based on a small overall error $\boldsymbol{e}$ and some additional considerations, as discussed in Section 2.3.

Once the most likely depth and its corresponding $\tilde{\boldsymbol{s}}_k$ have been determined, we compute frequency-dependent amplitudes and traveltimes: $\boldsymbol{s}_k$ and $\boldsymbol{u}_k$ of Fig. 1(e) are passband filtered to some passband b, as shown in 1(g). As in the broad-band case, the predicted and observed waveforms are then cross-correlated in order to estimate the (finite-frequency) traveltime anomaly $\tau_k^{(b)}$ and amplitude anomaly $a_k^{(b)}$. The optimal fit after both corrections is shown in Fig. 1(h).

2.2 Pre-processing: cluster analysis and temporal alignment

For global data sets with broad azimuthal coverage it often makes sense to subdivide the waveform data set into several, geographically distinct groups of stations. Instead of computing a single source time function for the global data set, we compute one function per group. This accounts for near-source effects with azimuthal dependencies and systematic regional traveltime anomalies. Pre-processing comprises three steps:

(i) quick and thorough quality control of the seismograms through cluster analysis,
(ii) decision on the number of separate groups to use,
(iii) temporal alignment of similar seismograms; this yields preliminary estimates of traveltime anomalies within groups.

The data that enter the cluster analysis are digital broad-band recordings of vertical ground displacement, sampled at a rate of 10 Hz. Waveform data from IRIS-DMC are deconvolved with their instrument responses and lowpass-filtered at 3.5 Hz. We use earthquakes of body-wave magnitudes 5.8 to 6.9; these events usually have sufficient signal-to-noise and relatively simple source characteristics. Epicentral distance ranges between 35 and 80 degrees, in order to avoid the P phase triplications at smaller distances and to ensure that the core-reflected PcP phase arrives well after P, pP, and sP. Parameter K in Table 1 indicates the number of seismograms that passed the quality control and cluster procedure for the 15 events used in this study.

A good general introduction to cluster analysis can be found in Kaufman & Rousseeuw (1990). In global seismology, the technique has been used on long-period data (Reif 2005), and on short periods by (Rowe *et al.* 2002). Starting out with $\tilde{K}$ windowed seismograms, the goal is to identify and subdivide the subset of K traces that are suitable for further processing. As measure of distance we use the $\tilde{K} \times \tilde{K}$ dissimilarity matrix $\boldsymbol{D}(k, l) = \boldsymbol{1}(k, l) - \boldsymbol{C}(k, l)$, where $\boldsymbol{1}$ is is equal to 1 everywhere, and $\boldsymbol{C}(k, l)$ is the cross-correlation coefficient matrix. The antisymmetric lag matrix $\boldsymbol{L}(k, l)$ contains the relative time lags at which maximum cross-correlation between traces k and l is achieved. Hierarchical linkage joins $\tilde{K}$ single objects into one large group in $\tilde{K} - 1$ consecutive steps. Similar objects are linked at an earlier step than less similar ones. The distance measure for linking composite groups is centroid (centre of mass) distance. Fig. 2 visualizes the order of linkage in a dendrogram (tree plot) for one of our sample events in the Aleutians (2000.112, $m_b = 6.0$).

The user needs to decide which traces to accept, and into how many groups to divide them. Selection is done interactively with a few mouse-clicks in the dendrogram. Identifying the rejects is usually easy. The decision about the number of groups N_g to use (i.e. the number of different $\boldsymbol{f}^{(g)}$ to compute) involves a trade-off in accuracy between relative and absolute traveltimes/amplitudes: Our method maps azimuthally dependent source effects into the source time function(s). A single source time function averages over azimuthal differences so that the overall fit of matched filters to data deteriorates for events with complicated source characteristics. For $N_g > 1$ regionally distinct groups, each of the N_g estimated functions will reflect different near-receiver effects (and other errors). Fits within each group improve but the question arises how well absolute amplitudes compare across groups.

Similarly, several smaller groups result in more accurate relative traveltime estimates. In the inversion procedure, all synthetic Green's functions are perfectly time aligned, and the same is implicitly assumed for the data. Therefore we align seismograms within each group g during pre-processing using VanDecar & Crosson's cross-correlation method. For larger N_g, seismograms are more similar and align more accurately within each group. However, this intra-group alignment introduces $N_g - 1$ free

Table 1. List of events used in this study. Dates are given as year.julianday and (month/day). Depths are given as the values obtained with our method, as well as the catalogue estimates. K is number of usable measurements for each event, given for the band that delivered the largest number of acceptable measurements. The rejection threshold was $C_x \leq 0.85$. N_g: number of data groups, that is, the number of source time functions computed. $\bar{c}_x$: median cross-correlation coefficient for the fit of broad-band matched filters to broad-band seismograms. N_R: number of usable measurements from the RISTRA array. N_{syn}: number of seismograms used in simulations, that is, permanent GSN stations within 35 to 80 degrees epicentral distance.

region	date	m_b	lat	lon	inv. depth	cat. depth	source	K	N_g	$\bar{c}_x$	N_R	N_{syn}
Costa Rica	1999.232 (08/20)	6.9	9.04N	84.16W	12 km	25 km	NEIC	108	1	0.97	13	40
Costa Rica	1999.233 (08/21)	5.8	8.92N	83.94W	12 km	15 km	HVRD	72	1	0.97	12	
Aleutians	2000.112 (04/21)	6.0	51.43N	177.80W	28 km	23 km	NEIC	170	2	0.94	35	80
Aleutians	2001.032 (02/01)	6.0	51.44N	177.80W	28 km	28 km	NEIC	106	2	0.93	40	
Panama	1999.362 (12/28)	5.9	5.61N	82.64W	6 km	17 km	NEIC	60	1	0.95	33	45
Panama	2000.347 (12/12)	6.1	6.01N	82.68W	4 km	17 km	NEIC	105	1	0.97	35	
Iceland	2000.169 (06/17)	6.5	63.97N	20.49W	2 km	14 km	NEIC	143	1	0.96	45	87
Iceland	2000.173 (06/21)	6.5	63.98N	20.76W	4 km	14 km	NEIC	167	3	0.92	42	
Laptev Sea	1996.174 (06/22)	6.2	75.74N	134.65E	12 km	15 km	NEIC	29	1	0.95		
Honshu, Japan	2001.083 (03/24)	6.8	34.08N	132.53E	50 km	49 km	NEIC	72	2	0.89		
Kuril Islands	2001.145 (05/25)	6.7	44.27N	148.39E	16 km	14 km	NEIC	116	2	0.96		
Aleutians	2001.165 (06/14)	6.5	51.16N	179.83W	10 km	11 km	NEIC	112	2	0.96		
Coast of Peru	2001.177 (06/26)	6.8	17.75S	71.65W	24 km	27 km	NEIC	64	1	0.98		
Kamchatka	2001.281 (10/08)	6.5	52.59N	160.32E	24 km	27 km	NEIC	42	1	0.98		
Alaska	2002.296 (10/23)	6.7	63.51N	147.91W	4 km	16 km	NEIC	39	1	0.96		

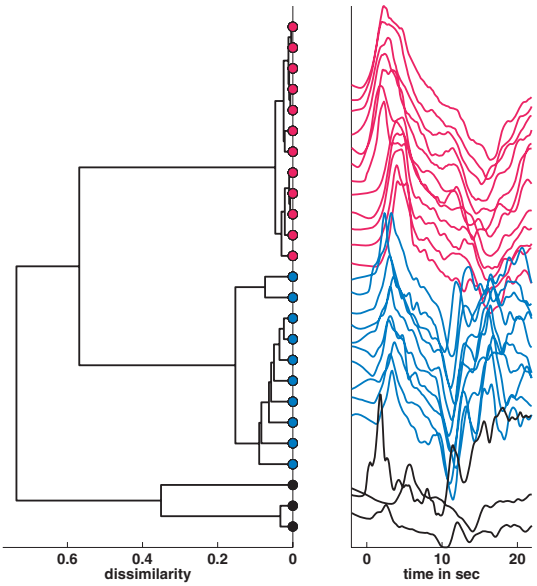

Figure 2. Dendrogram (cluster tree) and clustered traces of raw data, for Aleutian event 2000.112. The vertical leg of each [- shaped prong indicates the level of dissimilarity at which two objects are merged to form the next larger object. The eye easily discerns two main clusters, plus a few odd traces, which we eliminate from further analysis. Interactive picking by the user defines the number and extent of different groups to be used; this decision is indicated by the colouring. In this example, we chose to divide the data set into two large groups. The red traces form a very tight group; the blue traces are somewhat less similar to each other. Incidentally, all red stations are located in Eurasia, and all blue stations in North America, but no such prior knowledge is required or used. Rejected stations are colour black. For clarity, only a subset of the entire data for this event is shown.

parameters by leaving the groups' *average* delays floating relative to each other.

Many events are best treated as a single group of seismograms. In more complicated cases, a manageable approach that also achieves very good fits uses the dendrogram's first-order division into two or three groups of continental scale. For a small number of source time functions, check of inversion results is easily done by eye, as explained in Fig. 3.

2.3 Computation of the matched filters

The sizes of the data and parameter vectors in (2) mandate that the problem be linearized (matrix $\boldsymbol{A}$ is size (NK, N), where $N = 256$ and the number of seismograms K is up to 170 in this study). In his omnilinear inversion method, Ruff (1989) jointly inverts for $\boldsymbol{f}$ and a_k in a truly linear system, and excludes the trivial solution by imposing normalization constraints on $\boldsymbol{f}$ or a_k. Since we regard the moment tensor as an additional unknown, we solve (2) iteratively and without constraints on $\boldsymbol{f}$ or a_k, an approach that Ruff mentions as the 'bouncing method.' We initialize $a_k = 1$ for $k = 1, \ldots, K$; solving (2) for $\boldsymbol{f}$ by minimizing $\boldsymbol{e}$ is then a standard least squares problem with N unknowns, for which we use the LSQR algorithm (Paige & Saunders 1982; Nolet 1987). The damped solution is

$$\boldsymbol{f} = (\boldsymbol{A}^T\boldsymbol{A} + \epsilon\boldsymbol{J})^{-1}\boldsymbol{A}^T\boldsymbol{s}, \tag{3}$$

where ϵ is the model damping parameter, and $\boldsymbol{J}$ is an $N \times N$ diagonal matrix whose values increase linearly from zero to the average diagonal value of $\boldsymbol{A}^T\boldsymbol{A}$. This penalty on later samples favours short solutions and discourages oscillatory tails. If the data are divided into $N_g > 1$ different groups then (3) needs to be solved N_g times for the $\boldsymbol{f}^{(g)}$.

Now the source time function(s) can be assumed to be known. Minimizing $\boldsymbol{e}$ with $\tilde{\boldsymbol{s}}_k$ from (1) becomes a least squares problem with

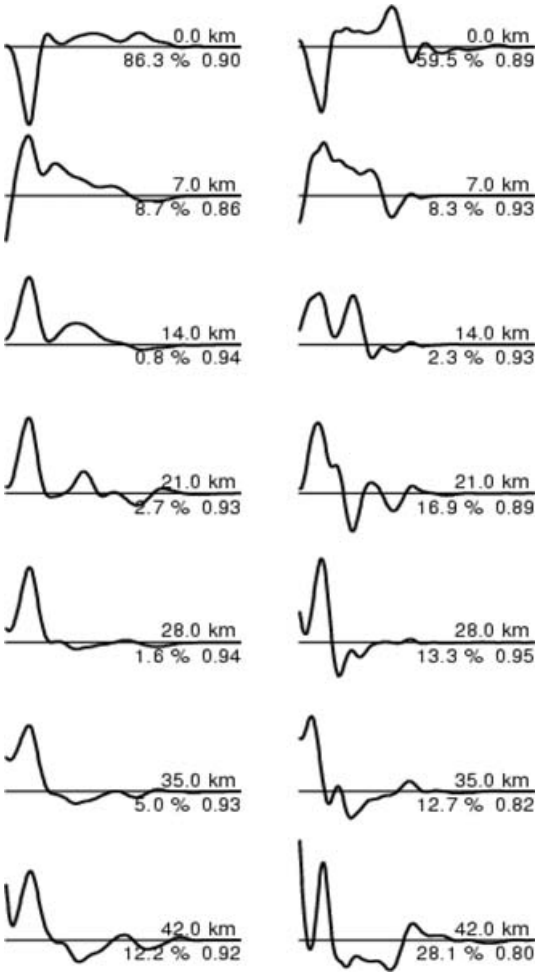

Figure 3. Output of matched filter computations: estimated source time functions for Aleutian event 2000.112 at different trial depths. Left column shows the source time functions obtained from seismograms in group 1 (Eurasia); right column shows source time functions for group 2 (North America). Indicated for every solution are focal depth, fraction of energy contained in negative samples, and median of cross-correlation coefficient (fit of matched filter to data). The rms error has its global minimum at 28 km. The choice of 28 km as most likely focal depth is also supported by the appearance of the two source time functions. The American and the Eurasian solutions are similar to each other, and they look 'simple', that is, compact, unimodal, and non-oscillatory. Another (local) minimum of rms error was found at 14 km; note how the two solutions for that depth are more complicated and less similar to each other.

a single unknown a_k; the solution is

$$a_k = \left(\boldsymbol{u_k}^T \tilde{\boldsymbol{s}}_{\boldsymbol{k}}\right) / \left(\boldsymbol{u_k}^T \boldsymbol{u_k}\right), \quad k = 1, \ldots, K \tag{4}$$

(This rms definition of amplitudes conforms to the definition used by Dahlen & Baig (2002) to compute amplitude kernels.) We iterate by inserting the new a_k into (2) and invert for the new $\boldsymbol{f}^{(g)}$. Then we update the a_k, and so on until the results converge or a break condition appears.

Optionally, we may also invert for a correction to the published moment tensor solutions. The moment tensor $\boldsymbol{M}$ can be regarded as a superposition of five linear dipole and double couple sources:

$$\boldsymbol{M} = \begin{pmatrix} m_1 & m_3 & m_4 \\ m_3 & m_2 & m_5 \\ m_4 & m_5 & -m_1 - m_2 \end{pmatrix}$$

Hence we compute each Green's function $\boldsymbol{g}_k$ as linear superposition of five partial Green's functions $\gamma_{k1}, \ldots, \gamma_{k5}$, each excited by a double couple:

$$\boldsymbol{G}_k = \boldsymbol{\Gamma}_{k1} m_1 + \boldsymbol{\Gamma}_{k2} m_2 + \ldots + \boldsymbol{\Gamma}_{k5} m_5 \tag{5}$$

The convolution matrices $\boldsymbol{\Gamma}_{ki}$ are constructed from the γ_{ki} in the same way as $\boldsymbol{G}_k$ is constructed from $\boldsymbol{g}_k$. Inserting (5) in (2) yields

$$\begin{aligned} \tilde{\boldsymbol{s}}_k &= a_k(\boldsymbol{\Gamma}_{k1} \boldsymbol{f}\ \boldsymbol{\Gamma}_{k2} \boldsymbol{f} \cdots \boldsymbol{\Gamma}_{k5} \boldsymbol{f}) \boldsymbol{m} \\ &= a_k(\boldsymbol{\upsilon}_{k1}\ \boldsymbol{\upsilon}_{k2} \cdots \boldsymbol{\upsilon}_{k5}) \boldsymbol{m}, \end{aligned} \tag{6}$$

where column vectors $\boldsymbol{\upsilon}_{ki}$ are the 'partial' equivalents of the predicted seismograms $\boldsymbol{u}_k$, and $\boldsymbol{m} = (m_1, m_2, m_3, m_4, m_5)^T$. We are trying to find a improved estimate $\hat{\boldsymbol{m}} = \boldsymbol{m} + \boldsymbol{\delta m}$ of the published $\boldsymbol{m}$. By rewriting (6) as

$$\begin{aligned} a_k(\boldsymbol{\upsilon}_{k1}\ \cdots \boldsymbol{\upsilon}_{k5}) \boldsymbol{\delta m} &= \tilde{\boldsymbol{s}}_k - a_k(\boldsymbol{\upsilon}_{k1}\ \cdots \boldsymbol{\upsilon}_{k5}) \boldsymbol{m} \\ \boldsymbol{\Gamma}\ \boldsymbol{\delta m} &= \boldsymbol{\delta \tilde{s}}, \end{aligned} \tag{7}$$

this again becomes a standard least squares (sub-)problem in the iterative loop. Initialize $a_k = 1$, invert first for the source time function(s) $\boldsymbol{f}$, second for $\delta \boldsymbol{m}$, third for a_k, and then reiterate until convergence or a break point is reached. Convergence means that the amplitudes or the rms error no longer change between iterations. A break condition is reached if the source time function develops a negative tail while the rms error decreases only minimally. Physically permissible source time functions are expected to be non-negative since fault rupture is thought not to reverse its direction during an event. However, the inversion will also map source-related effects, such as local reverberations, into $\boldsymbol{f}$ (i.e. we are using the term 'source time function' somewhat loosely here). For this reason it is unrealistic to expect a strictly non-negative $\boldsymbol{f}$. Fig. 3 shows solutions at different trial depths for the Aleutian example event. By default, the depth associated with the absolute minimum rms error is declared the preferred depth, although one can override this choice. In the majority of cases, that depth does coincide with the 'most reasonable looking' solution. Desirable qualities are simplicity, non-negativity, as well as similarity across groups if there is more than one group. Simplicity means that we prefer unimodal or short source time functions over bimodal or oscillatory solutions, provided that the rms error is not much larger for the simple solution. A certain amount of oscillation or negative tails is almost always present when inverting real data, but the depth region of small rms errors and the 'cleanest' looking solution usually coincide. Event 2000.112 in Fig. 3 provides an example for average data quality. For the most likely depth we cross-correlate and re-align each matched filter with its observation, thus improving on the VanDecar–Crosson estimates. Re-computing a_k on the newly aligned seismograms yields the final broad-band amplitudes.

2.4 Relative versus absolute (broad-band) traveltimes

In order to compute absolute traveltimes from the groupwise relative measurements we need to estimate any systematic delays common to all seismograms of a given group g. During processing so far, a systematic lag $\tau_0^{(g)}$ of the data w.r.t. the synthetics would have gone undetected as it would have simply shifted the onset of the source time function from $t = 0$ to $t = \tau_0^{(g)}$. Absolute traveltimes can thus be determined to the extent that the onsets of the N_g source time functions can be picked accurately. Alternatively, the absolute timing reference can be established by picking P-wave onsets on N_g groupwise stacks of ground displacements. We prefer the first method because the source time functions can be aligned relative

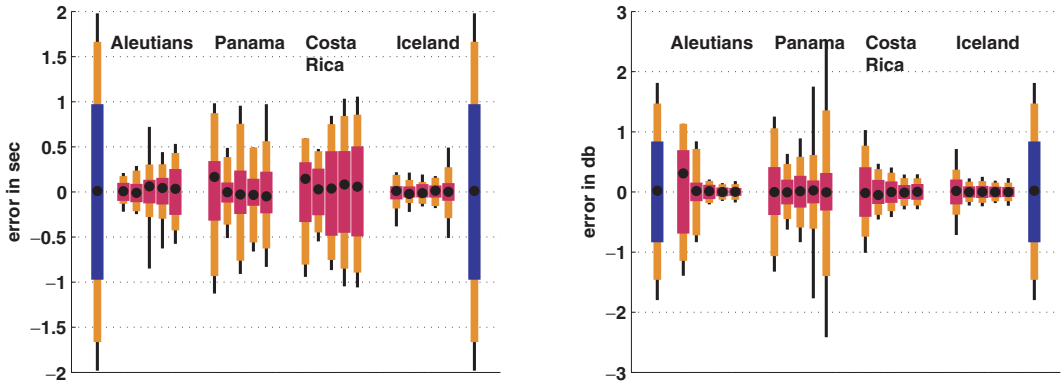

Figure 4. Results of tests on synthetic data. Recovery errors for broad-band traveltimes (left) and amplitude anomalies (right). For each of four events, 20 realizations were run at five different depths. Red bars denote the range in which 67 per cent of the measurements fall, orange and black bars denote the 90 per cent and 95 per cent ranges, respectively. Black dots mark the mean. Each event was simulated at five different source depths (5, 15, 25, 35 and 45 km), corresponding to the five vertical bars for each event, from left to right. 20 realizations were run for each depth, using randomized initial moment tensor estimates, traveltime and amplitude anomalies; for details refer to Section 3.1. The two outermost bars in each diagram show the distribution of the input anomalies: blue corresponds to the 67 per cent range, that is, standard deviation of 1 s in a normal distribution of traveltimes; the normal distribution for amplitude anomalies had a standard deviation of 0.8 db, that is, a factor of 1.2. In this figure and all following ones, amplitudes are plotted on a logarithmic scale: $a_{\mathrm{db}} = 10 \log_{10}(a_{\mathrm{lin}})$, where a_{lin} is the linear anomaly a_k of eq. (1).

to each other in an automated fashion, again using the VanDecar–Crosson method. This recovers $N_g - 1$ relative delays and leaves only one scalar (the common onset of the aligned source time function stack) to be picked manually. If source directivity has significantly dilated the source time function, one can attempt to undo this effect before time-aligning. Dilating each source time function by a bank of L trial factors $\alpha \approx 1$ generates a bank of $L \times N_g$ trial solutions. Cross-correlating each waveform with every other yields an optimal $\alpha_{n,m}$ from VanDecar–Crosson's equations, with $\log\ \alpha_{n,m}$ taking the place of the customary time delays $\tau_{i,j}$. In the simulations of Section 3.1, the onset picking error averaged over all events and depths was 0.19 s in the non-directional case, and 0.35 s in the directional case (it is included in Fig. 4). In practice, picking tends to be straightforward for small events and uncertain for large events with emerging onsets and complicated source characteristics. The decision of whether to actually use absolute traveltimes can be postponed until the time of tomographic inversion. At that time one can decide whether the absolute measurements are accurate enough to improve resolution over the traditional, prudent approach of solving for group time-shifts as independent parameters.

2.5 Finite-frequency amplitudes and traveltimes

Inputs for this step are the optimally time-aligned broad-band seismograms and matched filters. The $\boldsymbol{s_k}$ and $\boldsymbol{u_k}$ are bandpass-filtered using Kaiser (1974) window filters. The passbands can be chosen as convenient. Table 2 lists the frequencies and periods of the passbands that we use for this study. In each passband, every seismogram is re-aligned with its matched filter. We fit the first two to three oscillations of matched filters and data. Finite-frequency amplitudes are computed in the same way as for the broad-band data, see eq. (4). The bandwidth of the bandpass filter influences the structure of the Fréchet kernels for finite-frequency inversion. Wider passbands result in narrower kernels with less pronounced oscillatory sidebands.

The entire processing chain requires a few minutes of user supervision per event. Interactive input is needed in the cluster analysis and for the picking of source time function onsets. One also needs to check the appearance of the solutions at the automatically picked depth. The more time-intensive computations of the Green's functions and source time functions run fully automated in batch mode.

3 VALIDATION OF THE METHOD

Section 3.1 gives test results for various different source characteristics and receiver configurations. Tests on synthetic data provide the most controlled way of assessing the accuracy and robustness of amplitude and traveltime measurements. Readers mainly interested in real data may skip to Sections 3.2 and 3.3, where we analyse the 15 events of Table 2 and discuss evidence for wavefront healing.

3.1 Tests on synthetic data

We use synthetic data to assess the estimation accuracy of the following parameters: source depth, moment tensor, shape of the source time function, rms error, broad-band amplitudes, broad-band traveltimes. Recovery errors can be attributed to limited station coverage, initial errors in moment tensor, amplitude and traveltime estimates, as well as ambient noise and unknown source directivity

Table 2. Passbands for which finite-frequency amplitudes and traveltimes were measured. Bands are overlapping in a dyadic geometrical sequence: the centre frequency of band j is f_j; its corner frequencies $f_{j-1} = f_j/\sqrt{2}$ and $f_{j+1} = f_j\sqrt{2}$ are also the centre frequencies of the two adjacent bands.

band index	2	3	4	5	6	7	8	9	10	11
centre period in s	24.0	17.0	12.0	8.5	6.0	4.2	3.0	2.1	1.5	1.1
corner periods in s	34.0–17.0	24.0–12.0	17.0–8.5	12.0–6.0	8.5–4.2	6.0–3.0	4.2–2.1	3.0–1.5	2.1–1.1	1.5–0.8
centre freq. in mHz	42	59	83	118	167	236	333	472	667	943
corner freq. in mHz	29–59	42–83	59–118	83–167	118–236	167–333	236–472	333–667	472–943	667–1333

characteristics. The synthetic tests were designed to mimic four actual events in the Aleutians, Panama, Costa Rica and Iceland (2000.112, 1999.362, 2000.347, 1999.232). All of these are quasi-duplet events of particular significance in Section 3.3. The station set-up was that of the global GSN network, recorded at distances of 35–80 degrees; temporary deployments were not included. Synthetic seismograms were computed using the source time function obtained from the real event. The role of ambient noise was tested by adding to each synthetic seismogram a noise time-series recorded by the actual GSN station during an earthquake-free time interval. We also investigated the effects of inaccurate initial moment tensor estimates. The seismograms for each synthetic data set were computed from a moment tensor that deviated from the catalogue values according to a normal distribution with zero mean and a standard deviation of 5 degrees on strike, slip and dip. The iterative inversion was initialized with the catalogue value.

We ran 100 realizations of each event, with randomized source depths, traveltime and amplitude anomalies, and initial errors in the moment tensor. For a given run, the source depth used to generate the synthetic data was either 5, 15, 25, 35, or 45 km. Matched filters were computed for trial depths between 0 and 50 km, in increments of 1 km. Synthetic seismograms were time-shifted to simulate traveltime anomalies of normal distribution with zero mean and standard deviation of 1 s. They were also scaled to simulate normally distributed amplitude anomalies with a mean of one and standard deviation of ± 0.8 db, that is, a factor of 1.2, a value typical for events in our real data set.

For each simulated event, we compare recovery results for a scenario where source directivity is assumed to be negligible and for the case where it is a prominent effect. We first discuss the case without source directivity, where exactly the same $\boldsymbol{f}$ is used to generate the synthetic seismogram for each station. Fig. 4 shows errors in traveltime recovery (left), and errors in amplitude recovery (right); for a given event, the same source time function is used in all runs. Amplitude recovery error is defined as $E_a = 10 \log_{10}(a_{\text{out}}/a_{\text{in}})$, and traveltime error is $E_\tau = \tau_{\text{out}} - \tau_{\text{in}}$. Each vertical bar represents the spread of error for a certain event at a certain source depth. Each of the four events was simulated with a source at five different depths (5, 15, 25, 35 and 45 km); the same 20 initial moment tensors were used for all depths. For comparison of signal strength to recovery noise, the spread of the (normally distributed) input anomalies, τ_{in} and $10 \log_{10}(a_{\text{in}})$ is plotted at the left and right margins of each figure (the 67 per cent range is coloured blue).

Recovery results vary considerably between events, mainly as a function of density and azimuthal distribution of the recording stations. For the Aleutian and Iceland events there are 87 and 80 GSN stations within 35 and 80 degrees distance. The 67 per cent range of traveltime errors varies between 0.05 and 0.2 s for these two events; the 67 per cent range of amplitude errors is $\approx$0.1 db throughout, with the exception of a large error of 0.73 db for the Aleutian event at the shallowest source depth (more on this shortly). The Panama and Costa Rica events were 'recorded' by only 45 and 40 GSN stations, mostly in North America. The 67 per cent range is 0.1–0.5 s for traveltimes, and 0.1–0.25 db for amplitudes, which is still much smaller than the input anomalies of 1.0 s and 0.8 db.

Recovery of amplitudes tends to be less accurate at the shallowest depths. Amplitude estimates are more sensitive to mismatches in the waveform shape of the source time function than traveltimes, and shallow sources involve more ambiguity in deconvolving a source time function from seismograms that have their Green's functions' closely spaced pulses smeared into each other. The relatively large spread in amplitude errors at 5 km input depth is due to a limited number of runs with poor depth recovery. For the Aleutian event at 5 km input depth, the recovered depth is +4.2 km off on average, compared to less than 1 km at all other input depths. (It is not obvious however why the worst case occurs in this otherwise well-behaved event.)

The distribution of errors can differ significantly between runs for the same event at the same depth, especially if the event is badly constrained (Panama, Costa Rica). Again, heavy tails in the error bars of Fig. 4 are due to a limited number of bad runs, whereas such bad runs are largely absent in 'robust' events. In bad runs, iterations stop in local minima relatively far from the true depth, moment tensor. This happens mostly when the initial moment tensor estimate is strongly perturbed. The three unknown parameter vectors $\boldsymbol{f}$, $\boldsymbol{m}$, and a_k multiply each other in (6). Initial errors in $\boldsymbol{m}$ tend to be self-stabilizing, because any excess energy in the radiation pattern can be compensated by scaling down amplitude estimates in the affected region. Bad runs are usually easy to identify by the unlikely shapes of their source time function(s), that is, oscillatory behaviour and non-similar shapes across groups. (Average cross-correlation coefficients are lower also, but the difference may not be dramatic.) Initializing a run with the true moment tensor eliminates the largest part of the recovery errors. Initializing with a perturbed $\boldsymbol{m}$ but no amplitude or traveltime anomalies yields a smaller improvement. Starting out with the true $\boldsymbol{m}$, a_k, and τ_k yields near-perfect recovery ($-0.05\ s < \tau_k < +0.05\ s$, $0.98 < a_k < 1.02$), indicating that random noise is a minor source of errors. (Note however that signal-generated noise in the wake of the first phase arrivals is not modelled here.)

Even for a mediocre or bad run, relative delay and amplitude errors within groups are often small, even though group averages may show considerable systematic biases. One reason is that distortion of a source time function propagates into all of a group's matched filters in a similar way. Secondly, an error in the moment tensor causes a distortion to the radiation pattern that is spatially correlated on some length scale. Groupwise amplitude and traveltime biases also occur in real data and can serve as indicators for problems with the source time function and moment tensor inversion. The scatter in Fig. 4 decreases by 0.15 s and 0.1 db on average if we correct amplitudes and delays by their group means for every run; the improvement is largest for event/depth combinations with large error bars.

In a next step, source directivity is simulated by assuming unidirectional fault rupture with a velocity $|\vec{v}_R| = 0.9 v_s$, where v_s is PREM's S wave velocity at the source depth. For simplicity's sake, we assume horizontal rupture along the fault plane strike. A dilated $\boldsymbol{f}\ (\alpha_k\ t)$—rather than the original $\boldsymbol{f}(t)$—is used to generate each synthetic seismogram $\boldsymbol{s_k}$. The compression factor α_k is computed according to the Doppler formula $\alpha_k = (1 + w_k/v_p)/(1 - w_k/v_p)$. v_p is the P wave velocity at source depth, and w_k is the magnitude of the 'radial' velocity, that is, the projection of the rupture velocity vector $\vec{v}_R$ onto the ray's takeoff direction from the source. $\boldsymbol{f}$ is normalized to conserve energy. A station's epicentral distance affects the ray's takeoff angle and thus α. Dilation of the source time function is a non-linear effect and we do not attempt to recover α_k during inversion. The recovered solution(s) thus reflect averaged compression factors for each group. We dilate these solution(s) by a bank of different $\alpha \approx 1$, recompute the matched filters with those trial source time functions, cross-correlate with the data, and pick the α_k (and time delay) that yields the best fit. This procedure amounts to maximizing the wideband cross-ambiguity function of matched filter and data, a technique common in sonar applications (Flandrin 1999, Chapter 2.2 lists references).

Errors in amplitude and traveltime recovery largely follow the same patterns as for the non-directional case, but the magnitude of error increases. The 67 per cent range of traveltime errors is 0.1–0.6 s for the Aleutian event, 0.1–0.4 s for Panama, 0.4–1.1 s for Costa Rica, and 0.1–0.2 s for Iceland. For amplitude recovery errors, the 67 per cent range is 0.4–1.0 db for the Aleutian event, 0.2–0.4 db for Panama, 1.0–1.9 db for Costa Rica, and 0.1–0.6 db for Iceland. For Costa Rica and the Aleutian event at shallow depths, the signal-to-noise ratio in amplitude recovery is thus below 1. Note however that we have simulated a rather extreme case by assuming uni-directional rupture at $|\vec{v}_R| = 0.9v_s$: the pulse width of the solution could differ by a factor >3 for stations that are at 0 and 180 degrees of the strike direction. Since we limit ourselves to events of $m_b < 7$, real sources are more likely to rupture out in several directions from their nucleation region. None of the events in our real data set have yielded dilation factors as large as allowed for by the simulations.

3.2 Tests on global broad-band data

All events of Table 2 happened within 35 to 80 degrees from the Western United States; the selection aims at coverage of this region from all available azimuths. Eight of the earthquakes are special in that they come in pairs of quasi-duplet events ('quplets'). Comparing quplets provides a means of testing the accuracy of amplitude and traveltime measurements on real data. Since the waves take quasi-identical paths through the earth's mantle, the two independent measurements at the receiver should yield very similar traveltime and amplitude anomalies. Discrepancies between the measurements can then be attributed to shortcomings in the modelling. For our purpose, a pair of events qualifies as a quplet if they are shallow and the published epicentres are less than 50 km apart. For the quplet tests, we focus on events recorded during the deployment of the 950 km long passive RISTRA array (Colorado Plateau/Rio Grande Seismic Transect Experiment, Gao *et al.* (2004), Wilson *et al.* (2005)). The dense spacing and linear geometry of this long array allow us to investigate the spatial coherence of amplitude and traveltime patterns over hundreds of kilometres (Fig. 5).

Fig. 6 shows the yield of good measurements for the 15 events of Table 2. The left plot shows the range of cross-correlation coefficient c_x within which 67 per cent, 90 per cent, and 95 per cent of the observations fall, as a function of frequency band. Fig. 6, right, shows the number of seismograms for each band with a matched filter to data fit of $c_x > 0.85$ (visual inspection of waveform fits suggests this value to be a reasonable rejection threshold). Note that even in the absence of noise, $c_x = 1.0$ would occur only if there was neither diffraction nor wavefront healing; the distortions caused by these finite-frequency effects are interpretable with the theory of Dahlen *et al.* (2000). The fit of matched filters to data in the lowest bands is excellent ($c_x > 0.95$) and gradually decreases towards higher frequencies. Bands centred at 667 mHz and above yielded so few usable measurements that we do not consider them any further in this study. For the remaining bands, traveltime and amplitude statistics are plotted in Fig. 7; only observations with $c_x > 0.85$ are included.

The left plot shows the distribution of traveltime *dispersion*, that is, traveltimes are taken with respect to the broad-band traveltimes. It might seem more intuitive to use the highest or lowest passband as reference, but the power spectrum and measurement quality in the higher bands differs considerably from event to event. Overall, the broad band delivers the most stable measurements. Traveltime dispersion is largest for the lowest frequencies, on the order of 0.4 s

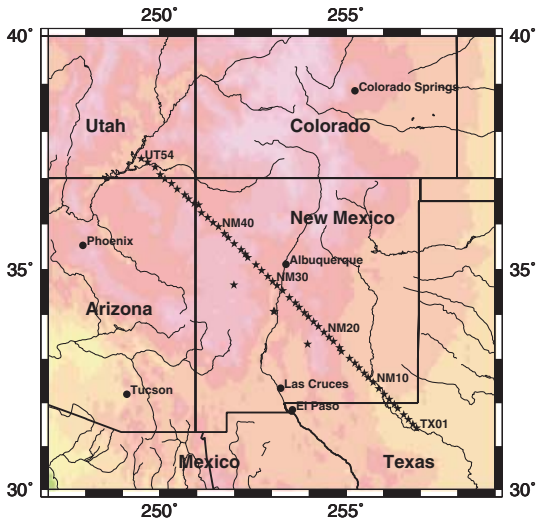

Figure 5. Topographic map with RISTRA (Colorado Plateau/Rio Grande Rift Seismic Transect Experiment) station locations. We used this dense, 950-km-long array to evaluate the accuracy of finite-frequency amplitude and traveltime measurements, and to look for spatial patterns across the tectonically active region. The passive PASSCAL experiment was deployed from 1999 to 2001 and consisted of 54 digital broad-band stations, running from Texas to Utah with an average station spacing of 18 km. Station indices start in the southeast (TX01) and end in the northwest (UT54). Three additional stations (55–57) located on magma bodies off the main line are not part of our data set.

for 67 per cent of the observations. This value drops to 0.2 s for the 83, 118, and 167 mHz bands, and further decreases to 0.15 s for the 236 and 333 mHz bands.

Amplitude anomalies show a stronger dependence on frequency; their spread increases towards higher bands. In the two lowest bands, 67 per cent of the amplitude anomalies are roughly within ±2 db, or a factor of 1.6, and 95 per cent of observations are within ±3 db, or a factor of 2. In bands centred at 333 mHz and 472 mHz, the ranges are ±3 db for 67 per cent of the observations, and ±5–6 db for 95 per cent of the observations. The amplitude average increases towards higher frequency bands. A (linear) trend of this kind could result from the observed *P* waves undergoing less attenuation than predicted by the PREM-attenuated Green's functions. An alternative explanation is amplitude amplification due to reverberations in low-impedance layers near the surface. Simulations by Zhou *et al.* (2003) show that amplification is approximately constant for wave periods longer than 6 s but increases with frequency for shorter waves. This could also account for the rising trend of Fig. 7, right. The spread of broad-band amplitudes is similar to the spread in the lower bands. Amplitude measurements are most reliable in the low bands (24–12 and 17–8.5 s ranges in particular). The overall energy content of the data is dominated by these bands; stacking the power spectra, we find corner frequencies between 1/20 and 1/7 Hz for the eight quplet events. At higher frequencies, part of the larger spread is likely due to larger measurement errors although analysis of the RISTRA quplets in Section 3.3 suggests that there is also more actual signal present.

3.3 Amplitude and traveltime patterns along the RISTRA array

The remaining figures compare measurement results for the RISTRA quplets. Fig. 8 shows broad-band traveltimes along the array

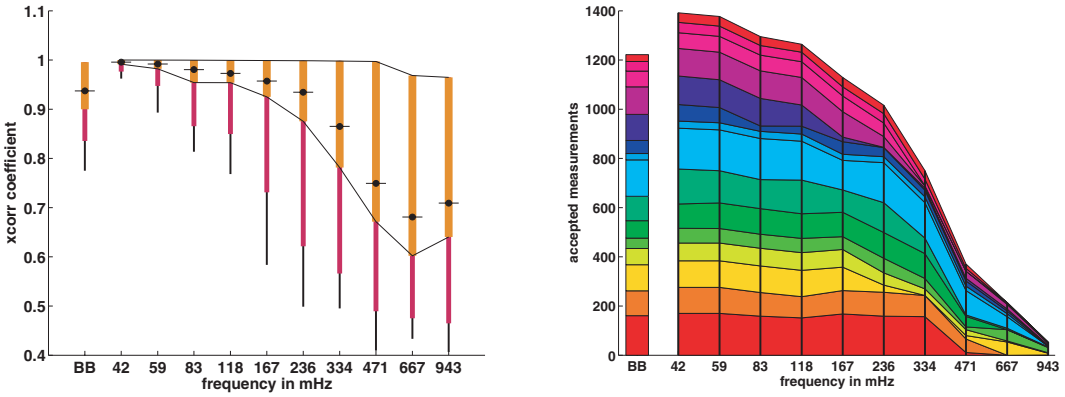

Figure 6. Frequency dependence of waveform fits for the 15 events studied. Left: cross-correlation coefficient for fit of data to matched filters. Each column is a simple histogram: the orange bar indicates the value range in which 67 per cent of observations fall, red and black bars span the 90 per cent and 95 per cent ranges. The black dot indicates the mean. Results for a frequency band j are plotted at its centre frequency f_j. Value ranges for the broad band are plotted to the very left, labelled 'BB'. Right: number of accepted measurements for each frequency band. A measurement is deemed acceptable if $c_x > 0.85$. Each coloured slice represents the contribution of one event, in the order of Table 1. Above 334 mHz, the number of acceptable measurements declines steeply. We therefore do not consider the two highest bands in the further analysis.

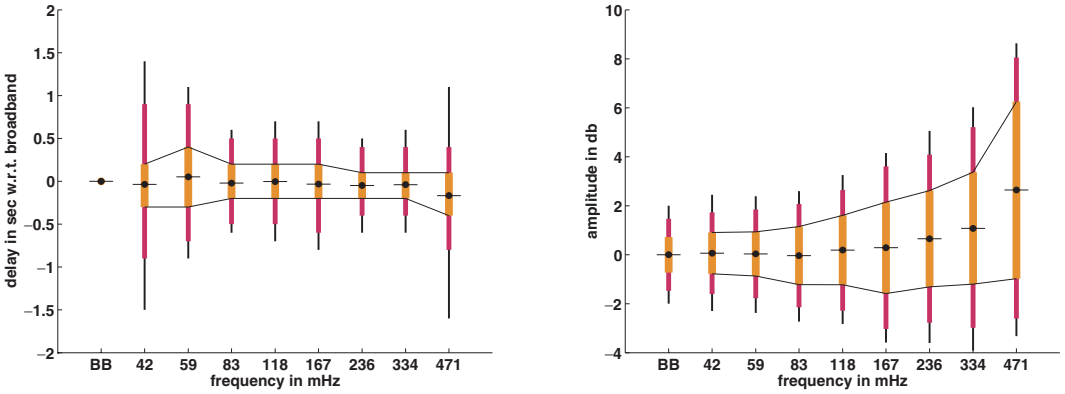

Figure 7. Traveltime and amplitude anomalies as a function of frequency band. Black dots mark the mean. Left: traveltime dispersion. Values are plotted relative to the traveltimes measured for the broad-band data; hence both the median and the spread for the broad band are zero. Right: deviation of measured amplitudes from predicted values. y-values of 1, 2, and 3 db correspond to amplitudes 1.2, 1.6, and 2.0 times larger than predicted. Orange, red, and black bars span the ranges in which 67, 90 and 95 per cent of observations fall.

for all four quplets, while Fig. 9 shows the broad-band amplitudes. Figs 10–13 are plots of finite-frequency observables. Finite-frequency traveltime anomalies and dispersion for the Aleutian and Panama quplets are shown in Figs 10 and 12, respectively. The corresponding plots for the Costa Rica and Iceland quplets can be found in the Supplementary Appendix S1 (available online). The left column of each figure shows traveltime anomalies with respect to PREM-predicted traveltimes, in different passbands. The right column plots traveltime dispersion, that is, the finite-frequency anomalies of the passband in question minus the broad-band anomalies of Fig. 8. Finite-frequency amplitude anomalies for these events are given in Figs 11 and 13 for the Aleutians and Panama. The same plots for Costa Rica and Iceland can again be found in the online Appendix S1. All plots follow the same format—see caption of Fig. 8. For each event, amplitude and traveltime anomalies are normalized by the broad-band averages of the station group that RISTRA belongs to (essentially the North American cluster); this facilitates visual comparison by eliminating possible offsets in the absolute amplitude and traveltime estimates. All measurements for which the broad-band c_x exceeded 0.85 were deemed acceptable; we also retain all corresponding passband measurements, even if their c_x decreases to less than 0.85 in the higher bands. The raw data that underlies all of these plots, namely waveform fits of seismograms to their matched filters in the different passbands, can also be found in the online Appendix S1.

Our observations on finite-frequency amplitudes and traveltimes along RISTRA are as follows:

(i) Usable frequency range: we achieve best measurement results in the period range between 24.0 and 2.1 s. Bands centred at 24 and 2.1 s are usable on a case-by-case basis. Measurement quality in higher bands is usually unacceptable due to cycle-skips, which cause timing errors on the order of the characteristic period of the band. A typical example is Fig. 10 bottom right, where the discrepancies are of order 2–2.5 s for stations 3, 50 and 51, and the centre period is 2.1 s. (Besides the fact that these measurements are wrong, the linearity assumption inherent in Fréchet kernel theory breaks down when delays are larger than one quarter of the wave period. Such large delays would therefore always have to be excluded from a finite-frequency inversion.)

(ii) The pattern of broad-band traveltimes in Fig. 8 is similar for all four quplets; it reflects the large scale tectonics of the RISTRA region. *P* waves arrive early on the southeastern end of the array, that is, in the Great Plains of Texas. Delays gradually increase towards

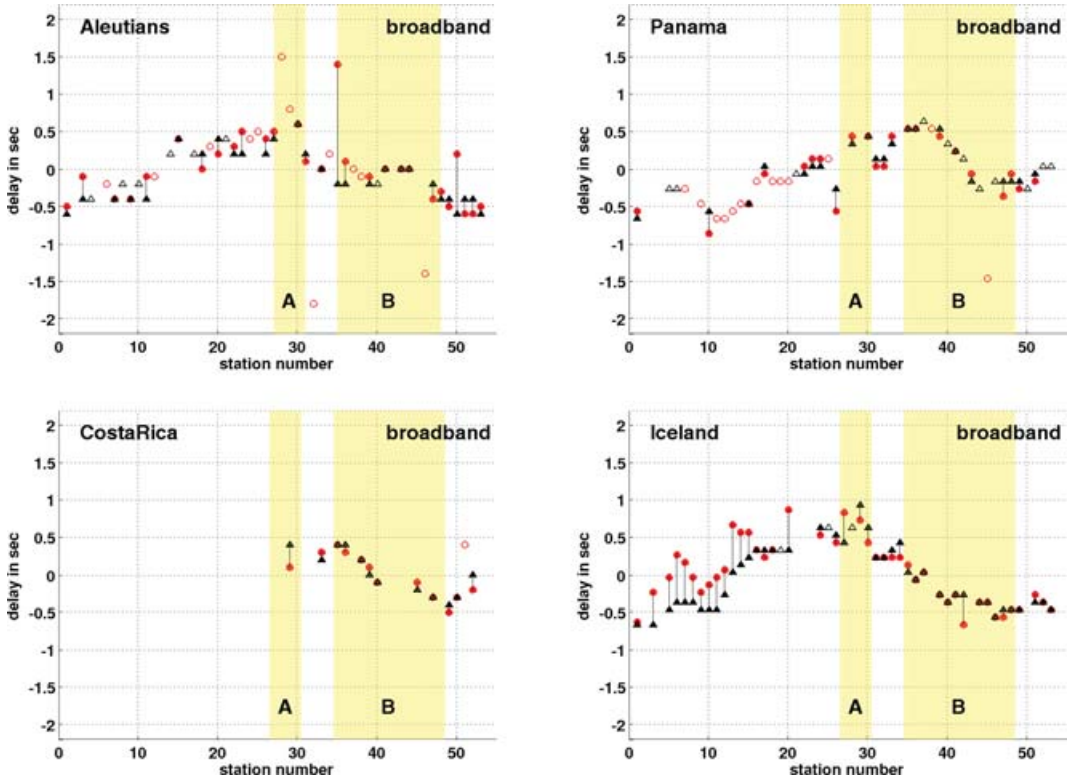

Figure 8. Broad-band traveltime anomalies along the RISTRA array for the four quplet event pairs. The *x*-axis plots RISTRA station indices, running from 01 in Texas to 54 in Utah. Red circles are observations for the first event of each pair in Table 1, black triangles correspond to the later event. If a station measured both events, the symbols are filled with colour and connected by a vertical bar. The first-order, rise-fall pattern of delays is common to all four events and reflects the regional tectonics: the array stretches from the seismically fast Great Plains across the slow Rio Grande Rift and onto the faster Colorado Plateau. The Aleutian, Panama, and Costa Rica quplets are incident roughly along the strike of the array. The waves from Iceland arrive almost perpendicular to it. Only the northwestern part of the array was deployed when the Costa Rica events happened. The shaded regions A and B are areas where traveltimes and amplitudes are strongly frequency-dependent (details in Figs 10–13).

the Rio Grande Rift (stations 23 to 30 were located in the rift). Arrivals gradually speed up again as one moves through a transition zone and onto the Colorado Plateau to the northwest. (The Costa Rica quplet was recorded only on this northern half of the array as the experiment was not yet fully deployed.) The difference between fastest and the slowest arrivals is on the order of 1.5 s for the six events that were measured along the full length of the array.

(iii) Consistency of broad-band traveltime measurements: The discrepancy between two quplet observations made by the same station is used as a proxy for measurement uncertainty. The average disagreement between measurements in Fig. 8 tends to be quite small (despite a few outliers). It is on the order of 0.2 s for the Aleutian quplet, and around 0.1 s for the Panama and Costa Rica quplets. The Iceland quplet produces near-perfect agreement on the northern half of RISTRA, but a systematic offset of around 0.4 s on the southern half (this phenomenon points to difficulties finding a moment tensor that fits all seismograms). All but a few of the single measurements (non-solid symbols) form smooth interpolations between the double measured stations, which gives us further confidence in the functioning of the method.

(iv) Broad-band amplitude anomalies (Fig. 9): there is no single large-scale pattern as for traveltime anomalies. However, we do observe spatial correlations over hundreds of kilometres, oscillating about the 0 db baseline in the range of ± 1 db. This kind of pattern would be expected for amplitude anomalies that are due to focusing. Acting like a lens, a curvature in the mantle's velocity field focuses energy to a certain area on the surface, while at the same time focusing it away from adjacent areas (conservation of energy). This would tend to generate a pattern of alternating high-amplitude and low-amplitude zones. However, spatial variations in asthenospheric Q could also explain the observed pattern.

(v) Consistency of broad-band amplitude measurements: Measurement discrepancies for amplitudes are larger than for traveltimes and vary considerably between quplets. For the Aleutian and Costa Rica quplets, the average disagreements are smaller than the average magnitude of the anomalies. While amplitude patterns for the two Panama events still show a clear spatial correlation, the measurement uncertainty is on the order of the signal itself. For the Iceland quplet, the measurement noise is larger than the signal. These differences in signal quality correlate with the complexity of processing the different quplets. The Aleutian and Costa Rica seismograms yield simple, unimodal source time functions at well-constrained depths. By contrast, we find that both Iceland earthquakes show more complex source characteristics than most. Their depths are not well constrained, and raw data as well as inverted source time functions have a complicated appearance, a view shared by Stefánsson *et al.* (2003) who have investigated these events in detail.

(vi) Finite-frequency traveltimes: For all quplets, finite-frequency traveltimes can deviate from their broad-band values by ± 0.5 s or more, as seen from the right columns of Figs 10, 12 and corresponding plots in the online Appendix S1. For all but the Costa Rican quplet, the lowest frequencies show the largest

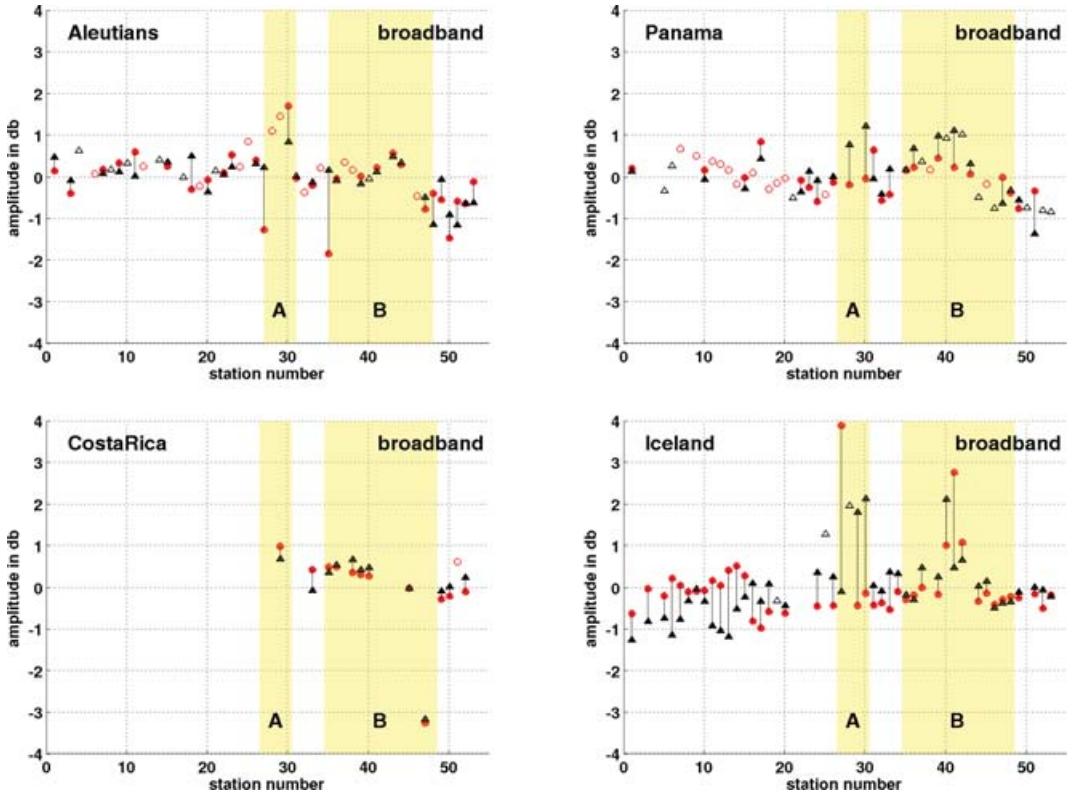

Figure 9. Broad-band amplitude anomalies along the RISTRA array. 1 db, 2 db, and 3 db correspond to amplification factors of 1.2, 1.6, and 2.0, respectively. Symbols as in Fig. 8.

deviations from the broad band. Dispersion gradually decreases towards higher frequencies; bands with dominant periods around 3–4 s are usually barely or not distinguishable from the broad-band traveltimes. These observations are consistent with Fig. 7, left. In scanning the left columns of Figs 10 and 12 from top to bottom, it is interesting to observe how the domelike pattern of traveltime anomalies gradually changes shape as a function of frequency. Measurement uncertainties in the range between 24 and 2.1 s track the uncertainties in the broad band. Average magnitudes of measurement discrepancies depend on the frequency band, but are in the range of 0.1–0.3 s for the Aleutian, Panama, and Costa Rica quplets; they are thus slightly larger than in the broad band. In the low passbands, this 'measurement noise' is smaller than the dispersion signal itself; in the higher bands both are on the same order. The Iceland quplet has higher uncertainties, as in the broad-band case. The consistency of measurements varies with frequency and location on the array.

(vii) Finite-frequency amplitudes (Figs 11, 13 and online Appendix S1) The magnitude range of amplitude anomalies grows as a function of frequency. For all four quplets, typical variations in the 24–12 and 17–8.5 s bands are of ± 1 db or less, whereas they span a range of ± 3 db between 6.0 and 1.5 s. Amplitude measurements are most consistent between 24–8.5 s: the measurement discrepancies are considerably smaller than the anomalies themselves in the case of the Aleutians and Costa Rica, and of the order of the anomalies for the Panama and Iceland events. As amplitude scatter grows with frequency, so do measurement discrepancies. The measurement error need not increase completely monotonously: for all but the Costa Rica quplet, measurement discrepancies in the 8.5–4.2 s and/or 6.0–3.0 s range (i.e. the microseismic noise band) are larger than in the next higher band(s). A good illustration is the bottom row of Fig. 11: amplitude scatter is comparable in both plots, but measurement discrepancies are much smaller in the higher band. In fact, the agreement in the 3.0–1.5 s band is quite good when compared to the magnitude of the anomalies.

(viii) Evidence for wavefront healing. The finite wavelength of a wave limits its resolving power. Wavefronts of longer waves heal more quickly as a function of distance from the perturbation. Attenuation, another dispersive effect, acts on amplitude and traveltime anomalies with the opposite sign: high frequencies are damped out more strongly. Amplitudes can also be amplified by low-impedance (sediment) layers close to the surface. In contrast to focusing, such amplification is a local station effect independent of the source azimuth.

We see two instances (termed regions A and B) of combined amplitude/traveltime patterns that suggest wavefront healing. Region A features narrow local maxima of both time delays and amplitude anomalies around stations 27–30. Broad-band and high-frequency traveltimes are delayed by 0.5 s and more at NM27 through NM30 for the Aleutian, Panama, and Iceland events (left columns of Figs 10, 12 and online Appendix S1). The same is not true for the low-frequency traveltimes. This can be seen by scanning the dispersion plots (right column) from top to bottom; we discuss the beautifully complete Aleutian data set in Fig. 10, but the same applies to the other two events. The top right plot shows a large negative pulse peaking at NM29; these lowest frequencies arrive almost a second earlier than the higher band frequencies (actually plotted are low frequencies minus broad band, but broad-band traveltimes become indistinguishable from finite-frequency traveltimes in some higher band(s)). At 17–8.5 s periods, the negative pulse is somewhat attenuated but still very evident; it is more attenuated at 12–6 s (not shown), and essentially gone at 8.5–4.2 s. In addition,

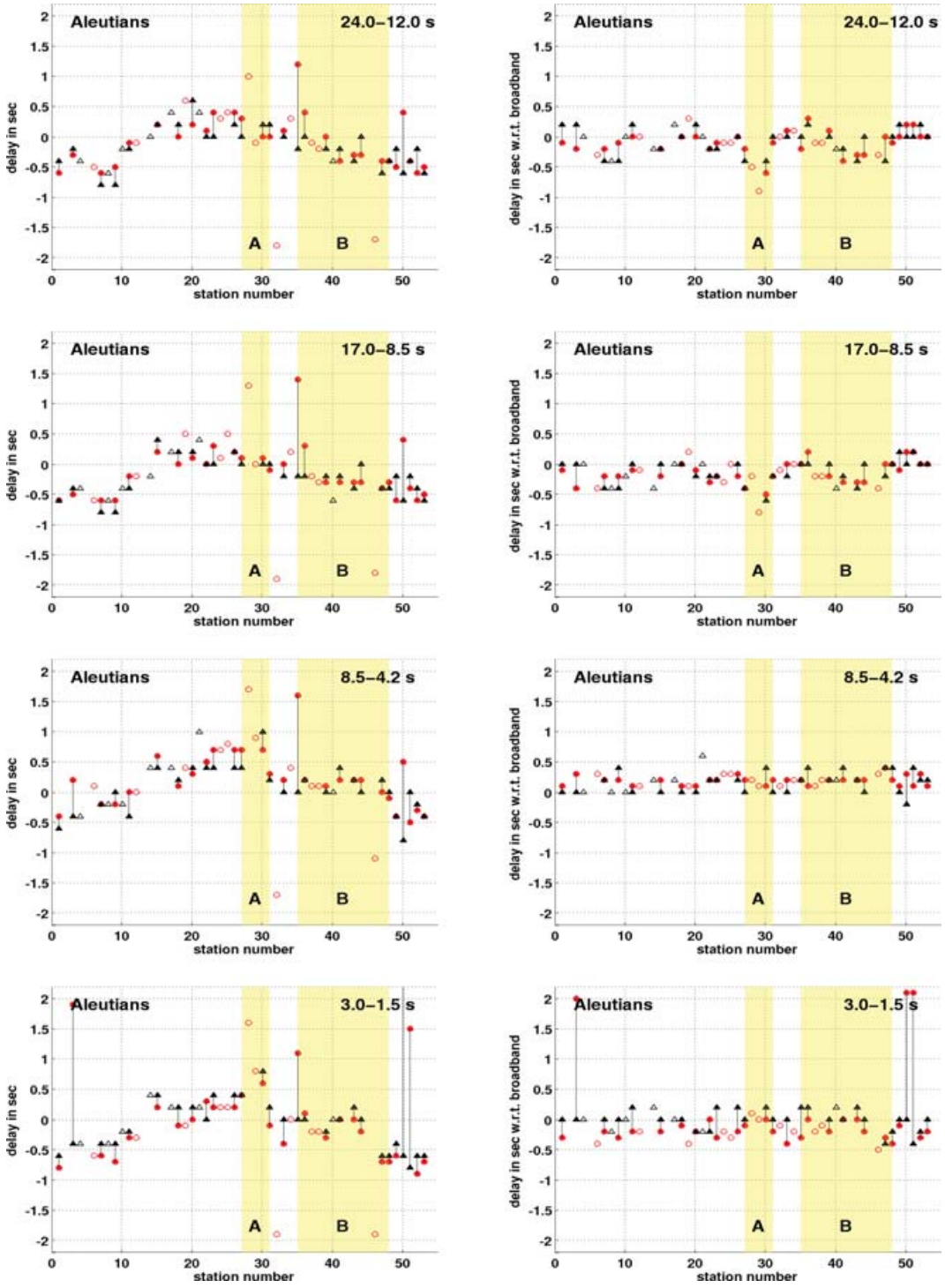

Figure 10. Aleutian quplet: finite frequency traveltime measurements along the RISTRA array. Left column shows traveltime anomalies in different bands, right column shows the corresponding traveltime dispersion, that is, the anomalies of the left column minus the broad-band anomalies of Fig. 8. Regions A and B stand out in terms of their frequency dependence, which is consistent across all quplets and suggests wavefront healing effects. (A) In the dispersion plots around stations 27–30, a sharp negative peak in the two lower bands gradually dies away towards the 8.5–4.2 s band, and reverses sign at even higher frequencies. The lowest frequencies arrive almost 1 s before the highest ones. (B) Around stations 37–47, similar behaviour as for A. The anomaly is spatially more extended but smaller in magnitude.

high-frequency amplitudes show a pronounced local maximum at stations NM28–NM30 for the three quplets in question (Figs 11 and 13 and online Appendix S1). Such an amplitude maximum is not or barely present in the lowest frequency bands.

Fig. 14 stacks the data of all four quplets; we compare amplitudes and traveltimes in a low-frequency band (period 17.0–8.5 s) to those in a high band (4.2–2.1 s). The dispersive signatures in regions A and B are robust and show up as positive peaks in the

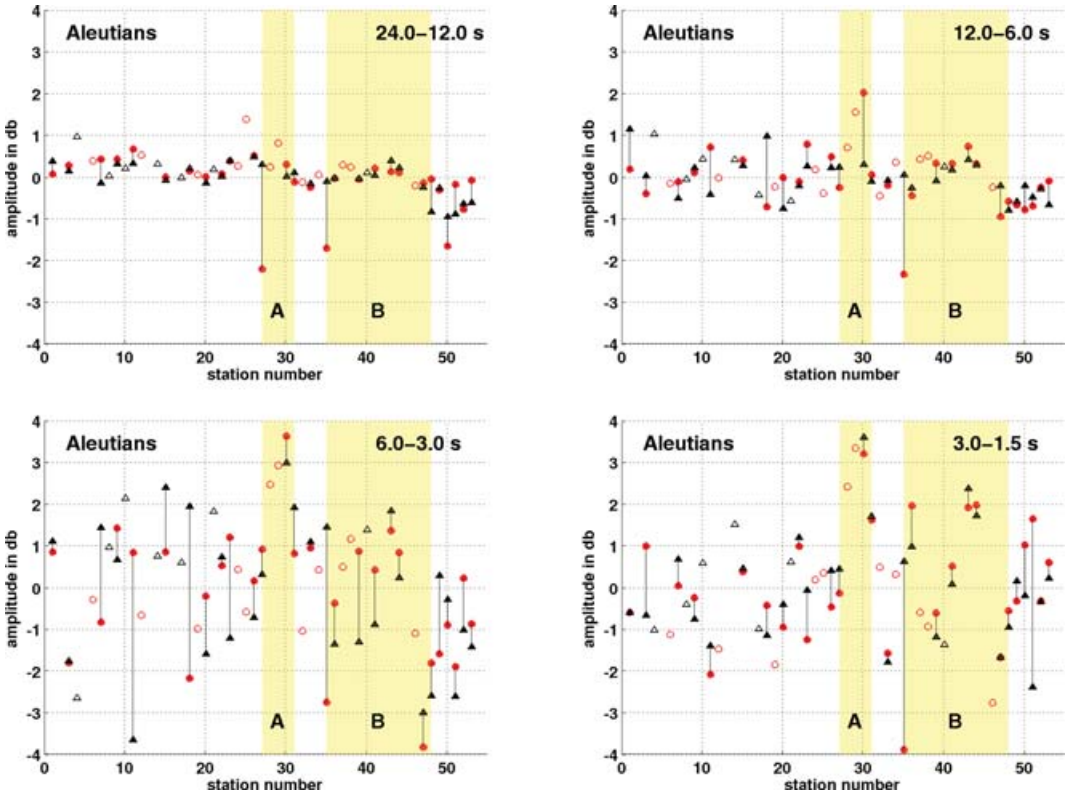

Figure 11. Aleutian quplet: finite-frequency amplitude recordings along RISTRA. Consistency of measurements is very good in the lowest band; one discerns a smoothly oscillating pattern with a spatial coherence of several hundreds of kilometres. In higher bands, both signal strength and measurement uncertainty increase. Uncertainties are largest in the microseismic noise band (e.g. the 6–3 s band). Region A: sharp positive amplitude anomalies at stations 28–30; strongest signal in high bands, gradually decreases towards lower frequencies. Region B: positive amplitude anomalies centred on stations 43/44, most pronounced at high frequencies; the sudden downward jump between stations 44 and 46 also occurs in the Panama and Iceland data.

amplitude plots, and also as peaks (not troughs) in the traveltime dispersion stack since we plot high frequencies minus low frequencies. The 2-D tomographic inversion of Gao *et al.* (2004) shows a very slow, localized anomaly under region A, where the Rio Grande rifting extends to the surface. This focusing structure at about 50 km depth can explain all observed dispersive effects. Energy is focused towards the central station NM29 to generate the amplitude maximum. Long waves heal more strongly than short waves, as seen in the delay and dispersion plots: arrivals in region A are delayed in general, but more so at high frequencies than at low frequencies. The width of peak A is roughly 50 km, which is also the approximate width of the most anomalous region in Gao's picture. Assuming an average P velocity of 6 km s^{-1} in the upper 50 km, wavelengths λ vary between 144 km for a centre period of 24 s, and 13 km for a centre period of 2.1 s. Scaling relations for wavefront healing (Nolet & Dahlen 2000) do predict strong wavefront healing effects for the geometry in question. Traveltime anomalies in the lowest bands are predicted to be two to four times smaller than those in the highest bands. (The uncertainty stems from the question whether their 2-D or their 3-D analytical solution for a Gaussian anomaly best approximates our geometry).

Region B features a roof-like amplitude pattern along stations 35–47. In the higher frequency bands, we see amplitude anomalies rise sharply towards a maximum around stations 40/41, then rapidly decline towards higher station numbers. This pattern is very prominent for the Panama, Iceland, and Costa Rica quplets (Fig. 13 and corresponding plots in online Appendix S1). It is less pronounced but still present in the lower frequency bands. In the Aleutian amplitude data (Fig. 11), the same pattern seems to be shifted to the northwest by a few stations (maximum at 43/44), suggesting some directional dependence. It is better visible in the lower frequency bands, which have better signal-to-noise ratio. In the higher bands, the dome-shaped amplitude pattern is pierced by a sudden downward jump, located between stations 44 and 46 for the Aleutians, 42 and 43 for Panama, and 45 and 46 for Iceland; this jump is very evident in Fig. 14 as well. Traveltime dispersion is strong in region B. A broad, trough-shaped negative dispersion anomaly at low frequencies heals towards higher bands. Arrivals in the lower bands are faster by about 0.5 s compared to the broad band. In the cases of Panama, Iceland, and the Aleutians, the trough minimum is centred on the very stations at which we see the maximum in the amplitude pattern (i.e. 40/41 for Panama and Iceland, 43/44 for the Aleutians). Some such directional dependence would be expected as the angle of wave incidence changes. Again a slow focusing structure could account for all observations. However, Gao's picture shows a fast anomaly below region B. A sedimentary surface layer could still explain the observed amplification of high frequencies but not the traveltime dispersion. The dispersion signal seems to originate at shallow depth: its (positively) peaked pattern in Fig. 14 is the same for all four quplets, whereas the traveltimes themselves strongly depend on event azimuth and must therefore be caused by deep anomalies. Waves incident from SE are more delayed than those from NW, a pattern that was also remarked on by Gao who stacked a much larger data set than ours. Possibly the extended fast anomaly

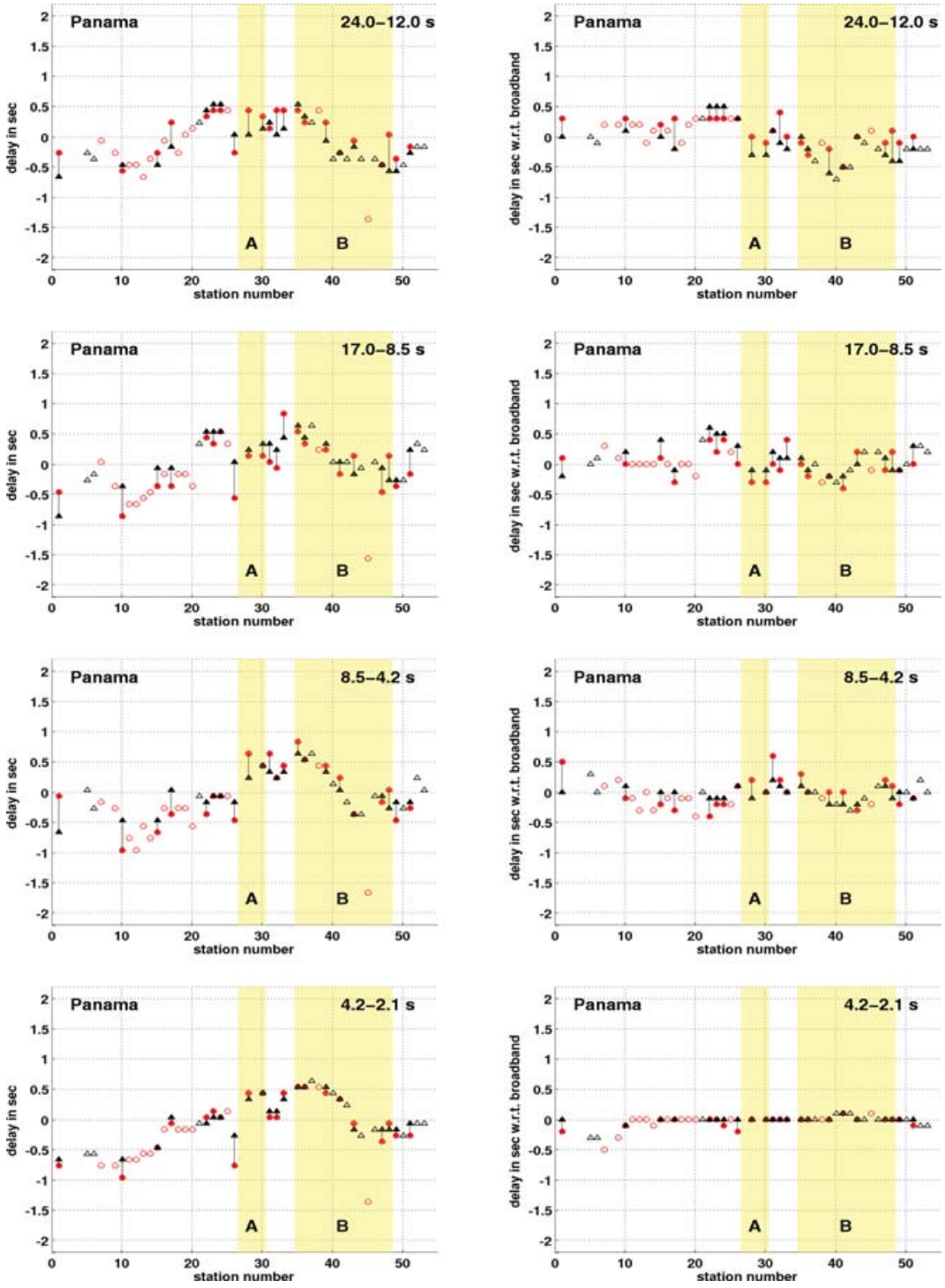

Figure 12. Panama quplet: finite frequency traveltimes (left column) and traveltime dispersion (right column), along RISTRA. Measurements from the two events generally agree very well. Region A: the negative dispersion anomaly around stations 28–30 is visible; no data for station 29. Region B: clear and broad negative dispersion anomaly centred on station 41, gradually dies away towards high frequencies. (Note that in this example, dispersion plots directly compare frequency bands since broad-band traveltimes are indistinguishable from those at the highest frequencies.)

under region B obscures a smaller slow anomaly immediately above it. Alternatively, the dispersion signal might be acquired from slow out-of-the-plane structure since the true sensitivity region around the source is finite, especially at low frequencies. 3-D tomography would be highly desirable to resolve this ambiguity.

4 CONCLUSION

The results of testing on synthetic and real data converge into a coherent picture. In synthetic tests, we recover the largest part of the input variance in amplitudes and traveltimes under all but the

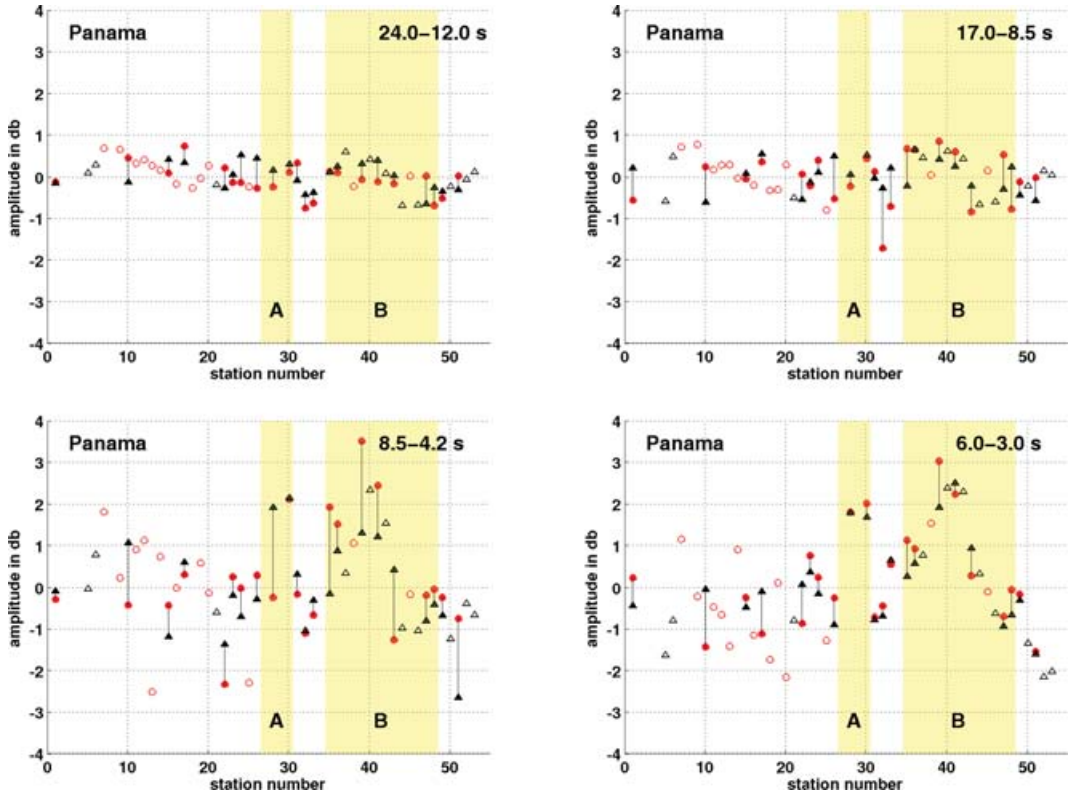

Figure 13. Panama quplet: Finite-frequency amplitude recordings along the RISTRA array. Region A: positive amplitude anomaly at stations 28 and 30, best visible at highest frequencies. Region B: strikingly clear manifestation of the roof-like, broad positive amplitude anomaly in the highest band, centred on stations 40–42; as for the Aleutian quplet, there is a sudden downward jump just north of the maximum. The magnitude of the amplitude anomaly gradually decreases towards lower frequencies.

most adverse circumstances. Estimation accuracy depends mainly on the density and azimuthal distribution of stations within the usable distance range. It also depends on errors in the moment tensor used to initialize the iterative matched filter inversion. Both kinds of errors complicate the recovery of source depth, which propagates into amplitude and traveltime errors. For real data, the average matched-filter-to-data fit in the broad band is between $x_c = 0.89$ and 0.98 depending on the event, with a median of 0.96. A future project is to investigate the influence of signal-generated noise and of azimuthally dependent source effects (other than Doppler shifts) on the accuracy of amplitude and traveltime measurements. However, given that cross-correlation values are already very good it seems fair to assume that this would yield significant improvements only for the most complicated events. In synthetic as well as quplet tests, the main indicators for badly constrained or otherwise problematic data sets are unlikely shaped source time functions (i.e. complicated, non-negative, and/or dissimilar source time functions across groups), as well as lower average cross-correlations. These indicators should be used in assigning *a priori* error bars to amplitude and traveltimes when routinely processing large data sets. Most complications are associated with large events ($m_b > 6.7$, roughly).

Traveltime dispersion in real data is on the order of 0.5 s in the wave period range from 24 s to 2 s. Broad-band traveltimes are more similar to those at the high-frequency end of this spectrum. Amplitude anomalies are on the order of 1 db in the lowest bands and 3 db in the highest bands, corresponding to amplification factors of 1.2 and 2.0, respectively. In two sections along the RISTRA array, we observe a combination of frequency-dependent amplitude and traveltime patterns that strongly suggest wavefront healing effects. Measurement uncertainties in the broad band are similar for synthetic and quplet tests. In synthetic tests, the standard deviation of the traveltime error varies between <0.1 and 0.5 s, depending on the event. Standard deviation for the amplitude recovery error is between 0.05 and 0.7 db. For the RISTRA quplets, measurement discrepancies for broad-band traveltimes are between 0.1 and 0.4 s within the North American group. Amplitude discrepancies are larger, but three out of four quplets still have SNRs between 1 and 3; errors are largest in the broad band and the microseismic noise band around 6 s. For non-quplet events in a tomography data set, we would assign *a priori* error bar values somewhere in the range found for the quplets; whether the values for a given event lie near the upper or lower end of the range will depend on the indicators discussed above.

ACKNOWLEDGMENTS

We are grateful to Rick Aster, David Wilson, and their collaborators on the PASSCAL/RISTRA experiment for making waveform data available to us in advance of the embargo deadline, and to Steve Grand for providing the data for the tomographic image in Fig. 14. We also thank Jeroen Ritsema and an anonymous reviewer for very helpful suggestions. This research was supported by the NSF under grant NSF/EAR 0309298.

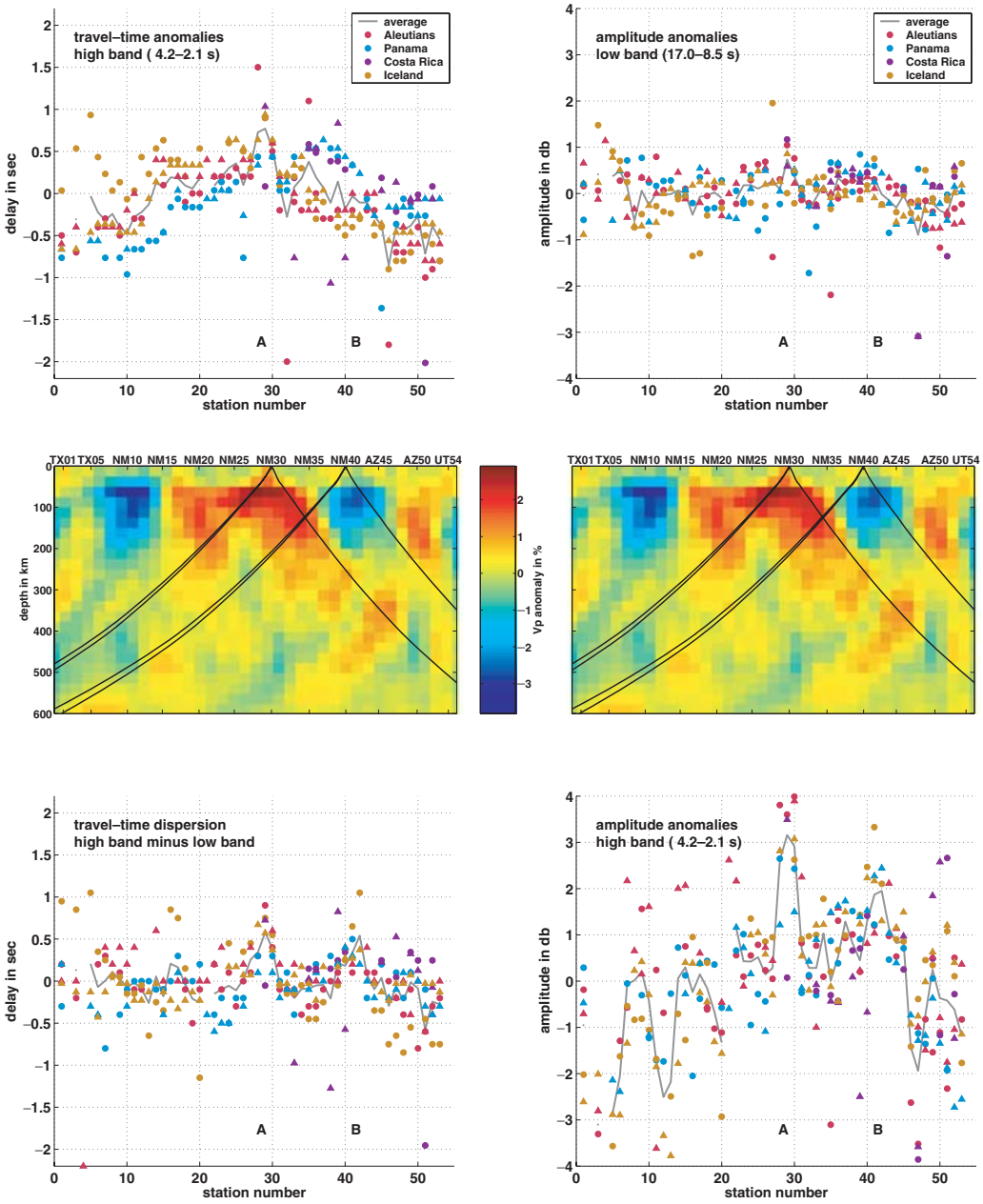

Figure 14. Traveltime and amplitude dispersion along the RISTRA array: comparison of all quplet data in a low-frequency band (17.0–8.5 s period) and a high-frequency band (4.2–2.1 s). Quplets are distinguished by colour, quplet events by symbols (◯ and △). Station averages are drawn as grey lines for stations that measured at least three out of eight events. Identical centre plots show the 2-D ray-theoretical *P* velocity model found by Gao *et al.* (2004). Black lines are sample ray paths to regions A and B from Panama and Costa Rica (from the left/southeast), and the Aleutians (from the right/northwest). The Iceland quplet has near-perpendicular incidence from northeast. Traveltime dispersion (lower left plot) shows a robust delay of high frequencies compared to low frequencies in regions A and B, as indicated by the positive peaks. Amplitudes are amplified in regions A and B, but much more so for high frequencies (lower right) than for low frequencies (upper right). This combination of dispersive effects suggests focusing and wavefront healing around localized, slow anomalies. Gao's inversion immediately supports this interpretation for region A, where Rio Grande rifting extends to the surface. The case for region B is less obvious. Traveltime dispersion stacks coherently for all four quplets, pointing to a shallow cause. By contrast, traveltime anomalies (upper left) strongly depend on incidence angle, indicating that most of the signal was acquired at depth. Possibly the extended fast anomaly imaged under region B is obscuring a smaller slow anomaly immediately above it, which manifests itself only through its stronger dispersive signature close to the surface.

REFERENCES

Chapman, C., 1978. A new method for computing synthetic seismograms, *Geophys. J. R. astr. Soc.,* **54,** 481–518.

Dahlen, F. & Baig, A., 2002. Fréchet kernels for body wave amplitudes, *Geophys. J. Int.,* **150,** 440–466.

Dahlen, F., Hung, S. & Nolet, G., 2000. Fréchet kernels for finite-frequency traveltimes—i. Theory, *Geophys. J. Int.,* **141,** 157–174.

Dziewonski, A. & Anderson, D., 1981. Preliminary reference earth model, *Phys. Earth planet. Inter.,* **25,** 297–356.

Flandrin, P., 1999. *Time frequency/time scale analysis,* Academic Press, San Diego, California.

Gao, W., Grand, S., Baldridge, W., Wilson, D., West, M., Ni, J. & Aster, R., 2004. Upper mantle convection beneath the Central Rio Grande Rift imaged by P and S wave tomography, *J. geophys. Res.,* **109,** B03305.

Haddon, R. & Husebye, E., 1978. Joint interpretation of P-wave time and amplitude anomalies in terms of lithospheric heterogeneities, *Geophys. J. R. astr. Soc.,* **55,** 19–43.

Iyer, H. & Hirahara, K., 1993. *Seismic Tomography—Theory and Practice,* Chapman and Hall, London.

Kaiser, J., 1974. Nonrecursive digital filter design using the i0-sinh window function, *Proc. 1974 IEEE Symp. Circuits and Systems,* pp. 20–23.

Kaufman, L. & Rousseeuw, P., 1990. *Finding Groups in Data: An Introduction to Cluster Analysis,* Wiley, New York.

Nolet, G., 1987. Seismic wave propagation and seismic tomography, in *Seismic Tomography: With Applications in Global Seismology and Exploration Geophysics,* pp. 1–23, ed. Nolet, G. D., Reidel, Norwell, Massachusetts.

Nolet, G. & Dahlen, F., 2000. Wave front healing and the evolution of seismic delay times, *J. geophys. Res.,* **105,** 19 043–19 054.

Paige, C. & Saunders, M., 1982. LSQR: An algorithm for sparse linear equations and sparse least squares, *ACM Trans. Math. Software (TOMS),* **8,** 43–71.

Reif, C., 2005. New Techniques for Analyzing Long-Period Seismic Data to Determine 3D Thermal and Compositional Structure of the Earth's Mantle, *PhD thesis*, Univ. of California at San Diego, California.

Ritsema, R., Rivera, L., Komatitsch, D., Tromp, J. & van Heijst, H., 2002. Effects of crust and mantle heterogeneity on PP/P and SS/S amplitude ratios, *Geophys. Res. Lett.,* **29,** 1430.

Rowe, C., Aster, R., Phillips, W., Jones, R., Borchers, B. & Fehler, M., 2002. Relocation of induced microearthquakes at the Soultz geothermal reservoir using automated, high-precision repicking, *Pure appl. Geophys.,* **159,** 563–596.

Ruff, L., 1989. Multi-trace deconvolution with unknown scale factors: omnilinear inversion of P and S waves for source time functions, *Geophys. Res. Lett.,* **16,** 1043–1046.

Stefánsson, R., Gudmundsson, G. & Halldársson, P., 2003. The South Iceland earthquakes 2000—challenge for earthquake prediction research, *Vedurstofa Íslands, Greinargerd 03017, 21 bls*.

Tibuleac, I., Nolet, G., Michaelson, C. & Koulakov, I., 2003. P wave amplitudes in a 3-D earth, *Geophys. J. Int.,* **154,** 1–10.

VanDecar, J. & Crosson, R., 1990. Determination of teleseismic relative phase arrival times using multi-channel cross-correlation and least squares, *Bull. seism. Soc. Am.,* **80,** 150–169.

Wilson, D., West, M., Aster, R., Ni, J., Gao, W., Grand, S., Baldridge, W. & Semken, S., 2005. Lithospheric structure of the Rio Grande Rift, *Nature,* **433,** 851–855.

Zhou, Y., Nolet, G. & Dahlen, F., 2003. Surface sediment effects on teleseismic P wave amplitudes, *J. geophys. Res.,* **108,** 2417.

SUPPLEMENTARY MATERIAL

The following supplementary material is available for this article:

Appendix S1. RISTRA finite-frequency amplitude and traveltime data for the Costa Rica and Iceland quplets, and raw waveform data underlying the finite-frequency measurements for all four quplets.

This material is available as part of the online article from: http://www.blackwell-synergy.com/doi/abs/10.1111/j.1365-246X.2006.03116.x (this link will take you to the article abstract).

Please note: Blackwell Publishing is not responsible for the content or functionality of any supplementary materials supplied by the authors. Any queries (other than missing material) should be directed to the corresponding author for the article.